GT2019-91172

DESIGN AND PROTOTYPE TEST DATA FOR A 300 KW AMB-SUPPORTED TURBINE GENERATOR FOR NATURAL GAS PRESSURE LETDOWN

Rasish Khatri
Calnetix Technologies
Cerritos, CA, USA

Larry Hawkins
Calnetix Technologies
Cerritos, CA, USA

Massimiliano Ortiz Neri
Nuovo Pignone
Baker Hughes, a GE company
Florence, Italy

Francesco Cangioli
Nuovo Pignone
Baker Hughes, a GE company
Florence, Italy

Davide Biliotti
Nuovo Pignone
Baker Hughes, a GE company
Florence, Italy

ABSTRACT

A 300 kW integrated and fully-sealed turboexpander-generator for natural gas pressure letdown (PLD) was developed by Baker Hughes, a GE company (BHGE), in conjunction with Calnetix Technologies. This paper describes the design and analysis of the generator, magnetic bearings, and touchdown bearings, with a focus on the dynamic performance and key characteristics of the machine. The permanent magnet (PM) synchronous generator is supported by PM-biased, homopolar magnetic bearings and has a maximum continuous operating speed (MCOS) of 31.5 krpm. A touchdown bearing system is implemented using rolling element bearings with soft mount supports. Also described is a thrust load balancing scheme that uses the thrust bearing coil current for reference. A time transient simulation showing the effect of process conditions on the AMB dynamics is shown. Preliminary data from the prototype mechanical run test are shown, including transfer functions measured using the magnetic bearings, Campbell diagram, and touchdown bearing drop test results.

INTRODUCTION

Industrial research on turboexpander technology has historically been aimed at developing high-efficiency machines that are well-qualified to meet the requirements of waste-energy recovery. Active magnetic bearings (AMB) and permanent-magnet high-speed generators (HSG) are a natural choice for such applications. In recent years, the Oil & Gas (O&G) industry has shown significant interest in converting waste energy in natural gas pipelines into electrical energy by installing turboexpander-generators in parallel with pressure let-down (PLD) stations [1]. The process of PLD is usually carried out by using a pressure regulator valve aimed at regulating the downstream pressure. This process leads to a significant amount of energy being dissipated as heat. Using a turboexpander instead of an expansion valve allows conversion of mechanical energy into electrical energy by means of a generator, while still reducing the gas pressure.

The machine developed by Baker Hughes, a GE Company (BHGE) together with Calnetix Technologies, consists of a 300 kW radial inflow turbine equipped with a fully integrated and sealed HSG running at 30 krpm rated speed.

The process of reducing the natural gas pressure has an undesirable side effect of decreasing the gas temperature at the outlet; this can lead to vapor condensation or hydrate formation. To overcome this issue, a typical solution is to use natural gas-fired boilers to pre-heat the gas before reducing its pressure. Moreover, the isentropic expansion, typical of a turboexpander, leads to a higher temperature reduction with respect to a common throttling valve which follows an isenthalpic expansion process. For this reason, the proposed machine has been equipped with a heat pump able to control both the inlet temperature and reduce the primary energy demand for gas pre-heating, as shown in Figure 1.

Thanks to the unique design of the direct-drive HSG, it is possible to select a versatile casing which is suitable for equipping different expander wheel sizes for different PLD stations. This results in a standard product which can be adapted to different station conditions.
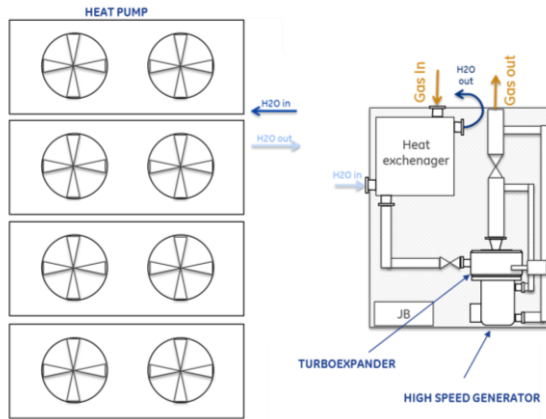
Figure 1. Expander-Generator plant arrangement

In this paper, the design and analysis of the HSG running on AMBs is described; many of the unique sub-systems, including the touchdown bearings and the thrust load balancing scheme are analyzed. A dynamic simulation of AMB under various process conditions is shown. Also, preliminary data from the prototype mechanical run testing and other design verification tests are reported and discussed. The test program carried out on the prototype expander leverages the experience of Calnetix Technologies and BHGE, as well as industry experience described in [2].

GENERATOR DESIGN

The generator and magnetic bearings were developed by Calnetix Technologies. Table 1 summarizes the basic design parameters for the PLD expander generator. The generator is a 4-pole, 16-facet permanent-magnet synchronous generator. The magnets are bonded to the rotor and retained by a shrink-fitted Inconel sleeve. The rated speed of the generator is 30 krpm and the maximum continuous operating speed (MCOS) is 31.5 krpm. The overspeed for the generator is 36.3 krpm.

TABLE 1. BASIC HIGH-SPEED GENERATOR PARAMETERS

Machine Type	4-pole, 16-facet, permanent magnet synchronous generator
Rated power (generating), **kW**	320
Stack **L**ength, **mm (inch)**	231.1 (9.1)
Rated Speed, **rpm**	30,000
MCOS, **rpm**	31,500
Over speed, **rpm**	36,300

A rotor stress analysis was performed to ensure the rotor could be spun continuously at 31.5 krpm, and could be spun temporarily at 36.3 krpm without risking loss of interference-fit between the sleeve and magnets. Additionally, a rotordynamics analysis was performed to ensure that the rotor bending modes were all greater than 125% of the MCOS, and that the rotor could be operated with a maximum synchronous

vibration of 25% of the backup bearing clearance from standstill up to MCOS. The rotordynamic model was also a primary component of the plant model used for magnetic bearing control design.

Figure 2 shows a layout of the PLD expander-generator, including some major aspects of the design. The generator uses a cooling jacket with a water-glycol mixture for heat rejection. There are two magnetic bearings, a radial magnetic bearing and a side-by-side combination (*SBS combo*) radial/axial magnetic bearing. The expander wheel is overhung on the SBS bearing-end of the shaft. This serves two purposes: 1) desired impeller axial position is more easily maintained in the presence of thermal growth, and 2) this configuration increases frequency of the first rotor bending mode, providing additional rotordynamic separation margin. The rotor is designed to grow (due to thermal expansion) towards the non-turbine end (NTE) of the shaft.
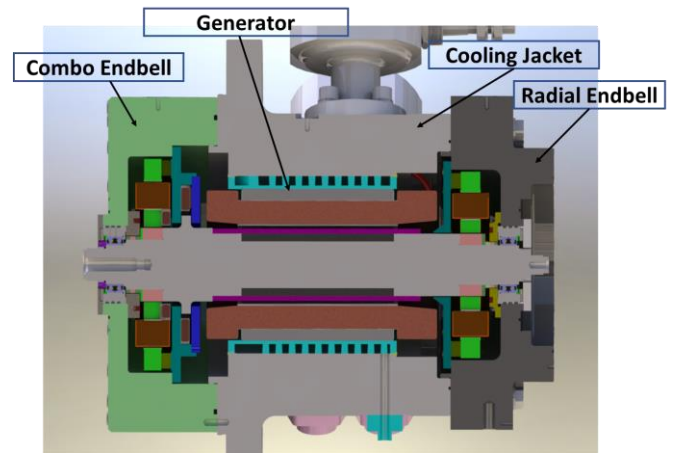

Figure 2. Generator layout showing cooling jacket and magnetic bearing endbell assemblies

Figure 3 shows both magnetic bearing assemblies. The radial magnetic bearing assembly contains a two axis (*x1*, *y1*) radial actuator, two radial position sensors, a speed sensor, and a resiliently mounted radial backup bearing. The combination magnetic bearing assembly contains the three axis (*x2*, *y2*, *z*) SBS combo actuator, two radial position sensors, an axial position sensor and resiliently mounted radial/axial backup bearing. The radial magnetic bearing is also called *bearing 1* (or *radial bearing 1*) and the SBS combination magnetic bearing assembly is also called *bearing 2*. This paper refers to the portion of the SBS combination actuator which controls the axial motion as the *axial bearing*. The portion of the SBS combination actuator which controls the radial motion is aso called *radial bearing 2*.

The radial sensors are inductive sensors and the axial edge sensor uses a flux density sensing coil to pick up axial displacement from a radial surface. The operating principles of

the radial and axial sensors have been previously described in detail by Filatov [3], [4].

The actuators are homopolar, permanent magnet (PM)-biased AMBs. More information about the mechanical arrangement and characteristics of the radial and side-by-side (SBS) combination radial/axial actuators can be found in both [5] and [6]. The actuators are driven by a magnetic bearing controller (MBC). ==
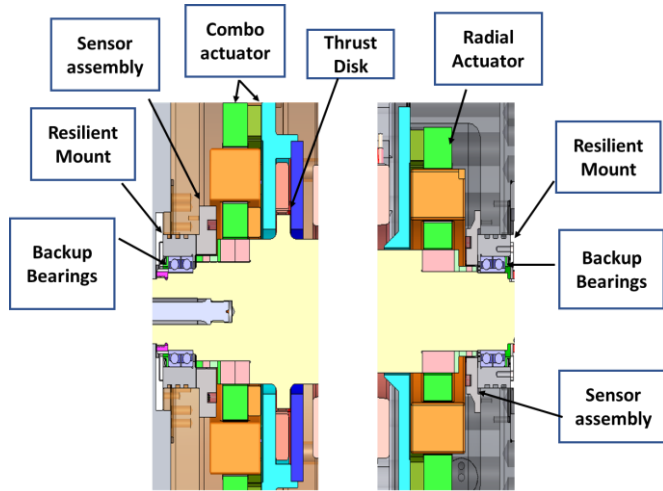

Figure 3. Detail of magnetic bearing endbell assemblies, showing the combination actuator endbell (left) and radial actuator endbell (right)

Table 2 summarizes the minimal design parameters for the magnetic bearing actuators. The radial bearing is designed to carry a 1005 N (226 lbf) load with a nominal air gap; the minimum design requirement was 875 N (196 lbf). The radial bearing that is part of the combo bearing arrangement is designed to carry a 1067 N (240 lbf) load with a nominal air gap; the minimum design requirement was 910 N (204 lbf). The axial bearing is designed to carry 3069 N (690 lbf) with a nominal air gap; the minimum design requirement was 2620 N (587 lbf). The unique design of the SBS combo actuator results in a reduced thrust disk diameter compared to conventional axial AMBs; this results in reduced windage losses [7].

TABLE 2. BASIC MAGNETIC BEARING DESIGN PARAMETERS

Parameter	Radial, Brg 1	Radial, Brg 2	Axial
Minimal load capacity, N (lbf)	875 (196)	910 (204)	2,620 (587)
Force constant, N/A (lbf/A)	123 (27.6)	139 (31.2)	357 (80.1)
Negative stiffness, N/mm (lbf/in)	1,300 (7,420)	1,240 (7,080)	1,210 (6,900)
Magnetic air gap, mm (mils)	1.40 (55)	1.40 (55)	1.02 (40)
Slew corner frequency, Hz	129	120	40

Figure 4 shows the predicted load capacity versus frequency curve for the axial bearing, normalized to the static load capacity. There are two main contributing factors to the reduction in load capacity versus frequency: 1) the fixed amplifier overhead voltage limits the maximum current slew rate, and 2) eddy currents generated in the actuator due to the use of non-laminated magnetic paths (common to all industrial axial magnetic bearings). As such, the axial bearing can only achieve its maximum load capacity when reacting purely static loads. At 100 Hz, the axial load capacity is decreased to approximately 20% of the static load capacity.
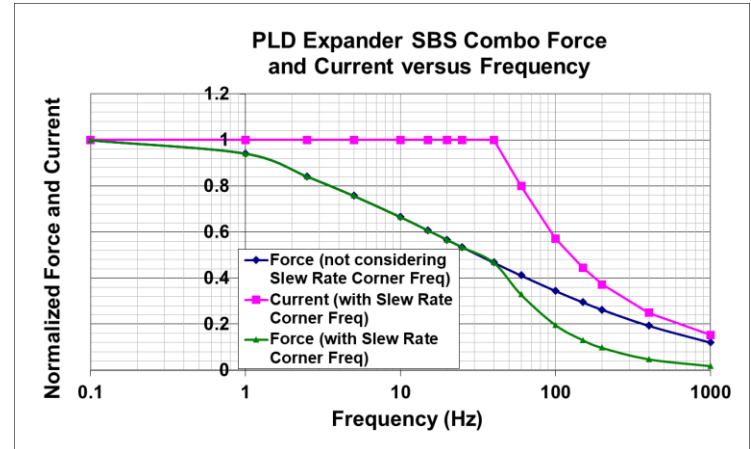

Figure 4. Axial load test results

A load test was carried out on the PLD expander prototype axial and radial bearings to measure the maximum static load capacities of the actuators. Figure 5 summarizes the results of the axial load test. The maximum axial load exceeds 2,620 N (587 lbf) in both directions, and thus exceeds the required load capacity of the bearing. There is a small (~110 N) offset in the measured data for the 0 A line. This implies that the levitation position of the thrust disk is not at the magnetic center of the axial bearing. This is normal as the control set point is placed so that the rotor levitates at the backup bearing central position.
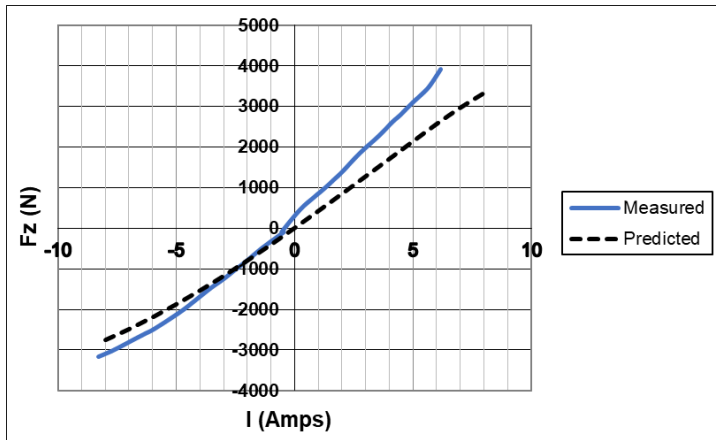
Figure 5. Axial static load test results

Figure 6 summarize the results of the radial load test. The maximum loads on bearing 1 and bearing 2 exceeded the design requirement of 875 N (196 lbf) and 910 N (204 lbf), respectively.
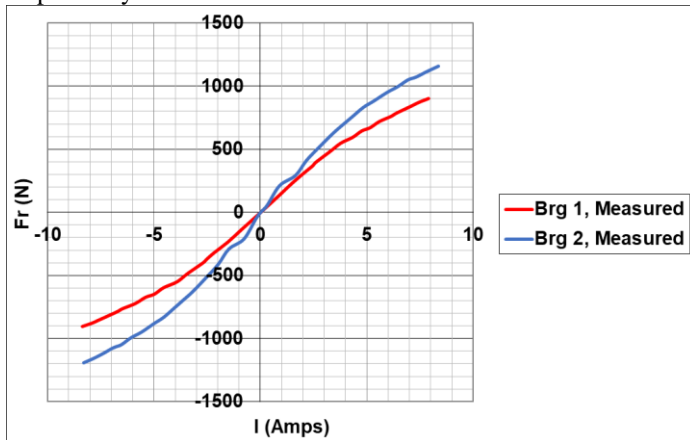

Figure 6. Radial static load test results

ROTORDYNAMICS AND DYNAMIC CONTROL SYSTEM ANALYSIS

A rotordynamics analysis was carried out for the PLD expander. As mentioned earlier, the rotordynamics analysis was intended to ensure that the rotor bending modes were all greater than 125% of the MCOS. Figure 7 shows the geometry of the rotor with the material property assumptions of each station used for the analysis. All interference-fit components were modeled with zero stiffness, a conservative assumption. The impeller weighs 5.19 kg and is constructed of titanium. Table 3 summarizes the mass properties used for the impeller.

Figure 8 shows the free-free natural frequency map of the rotor and Table 4 summarizes the frequencies of the first three bending modes. The rotor is predicted to operate below the 1st critical speed with a predicted margin of 46.0% at the nominal speed of 30,000 rpm. The rotor is expected to operate

close to the 1st backward bending mode; this is unlikely to have a significant impact, as backward modes are not typically excited by rotor unbalance.
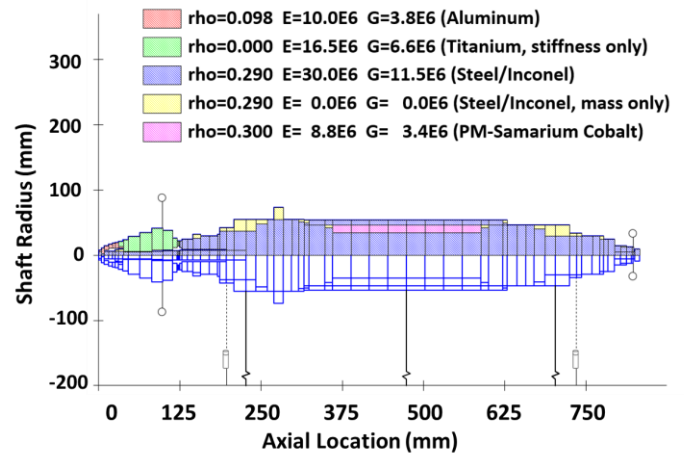

Figure 7 Rotor Model (turbine, thrust disk, and radial bearing 2 are on the left side; radial bearing 1 is on the right side)

TABLE 3. IMPELLER MASS PROPERTIES

Material	Titanium
Mass	5.19 kg (11.44 lbm)
Ip	23,583 kg-mm^2 (80.59lb-in^2)
It	14,093 kg-mm^2 (48.16 lbm-in^2)
CG - from shaft interface	26.3 mm (1.037 in)

When the rotor speed is greater than the 1st backward bending mode frequency, rotor internal friction/dry friction rubbing can excite a backward mode. However, the AMB compensator is designed with positive damping near the 1st backward bending mode frequency to ensure that this mode is stable when the rotor is levitated. It is worth noting that a backward mode may be excited during a rotor drop event at speed due to dry friction.
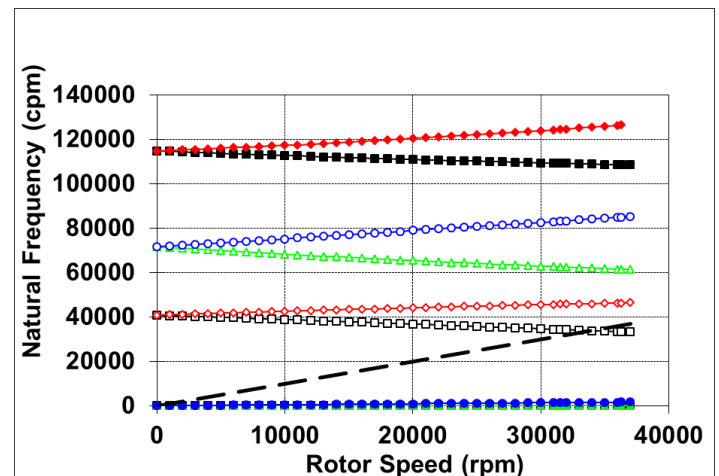

Figure 8. Free-Free Natural Frequencies of PLD expander

TABLE 4. ROTOR BENDING MODES

	1st Forward Bending Mode (cpm)	Margin to 1st Forward Bending Mode	2nd Forward Bending Mode (cpm)	3rd Forward Bending Mode (cpm)
Nominal SPD (30kRPM)	43,806	46.0%	80,949	122,286
MCOS (31.5kRPM)	43,985	39.6%	81,491	122,852
Overspeed (36.3kRPM)	44,537	22.7%	83,177	124,727

Figure 9 shows the first free-free bending mode shape. This mode is driven by the overhung expander wheel mass and the stiffness of the generator magnet section. The first bending mode has a node close to the sensor of bearing 2 and as such that bearing 2 will have little influence on this mode. This characteristic makes the control algorithm for bearing 2 somewhat simpler as will be discussed later.
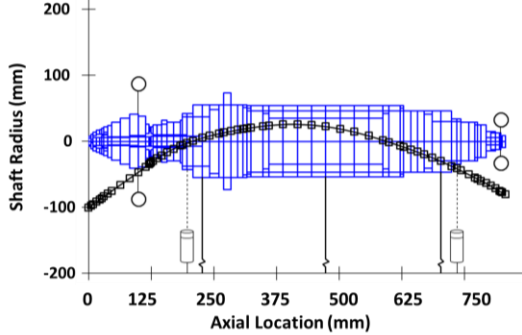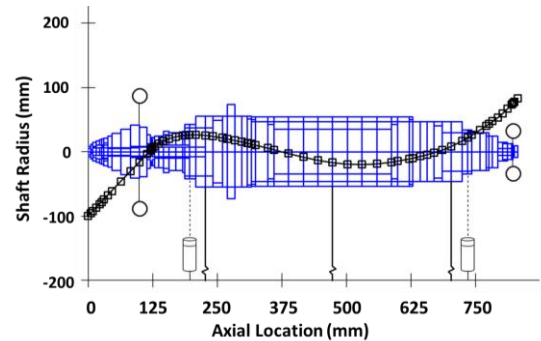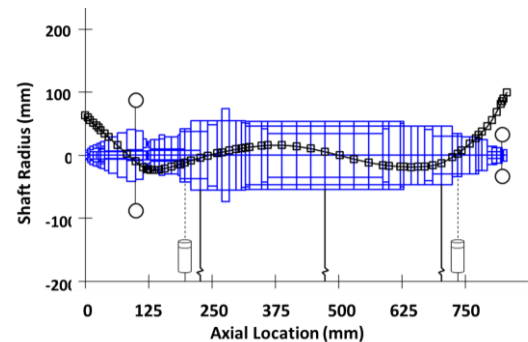

Figure 9. 1st bending mode shape

Figures 10 and 11 show the second and third bending mode shapes, respectively. The second bending mode shape has a node near the bearing 1 actuator. This mode is driven by the stiffness at the combo backup bearing section of the rotor, the stiffness of the tie-bolt tying the expander wheel to the rotor, and the stiffness on the NTE of the generator rotor. This mode is not as influenced by the impeller wheel mass as the first bending mode is. While this mode is not heavily influenced by the wheel mass, the ratio of the polar moment of inertia (I_p) to the transverse moments of inertia (I_t) has a large impact, due to the large *conical* motion observed through the center of gravity of the wheel for both modes. A larger I_p/I_t increases the effective stiffness of the rotor with increasing speed for forward-whirl bending modes and decreases the effective stiffness of the rotor with increasing speed for backward-whirl bending modes. This effect is seen earlier in Figure 8 in all three modes, but most heavily for the second bending mode.

The third bending mode shape has a node at the bearing 1 sensor and little modal displacement at the bearing 1 actuator. This mode also has little modal displacement at both bearing 2 actuator and sensor axial positions. Similar to the 2nd bending mode, the 3rd bending mode has little modal

displacement near the expander wheel center of gravity and is thus not significantly influenced by the wheel mass.

The rotordynamics of the prototype generator, shown in Figures 12-15, were characterized by measuring the plant and sensitivity transfer functions, using the AMB actuator as a dynamic exciter. The plant transfer function includes the dynamics of the rotor/housing, sensor, actuator, and amplifier. A dummy wheel was installed to the rotor, representative of the mass properties of the actual expander wheel. The seals were not installed during the mechanical run test. Refer to [8] for the complete definitions and interpretations of the magnetic bearing plant and sensitivity transfer functions.

Figure 12 shows the measured plant transfer function for radial bearing 1 and radial bearing 2 at 0 rpm. There are three distinct bending modes seen in the plant transfer function. The plant transfer function shows a significantly larger 1st bending mode gain on bearing 1 than on bearing 2. This is because the modal displacement near bearing 2 is quite small compared to that near bearing 1, as shown earlier in Figure 9. For the 2nd bending mode, the gain on bearing 2 is larger than the gain observed on bearing 1. This is also explained by the differences in the modal displacements at each radial bearing, as observed in Figure 10.

Figure 10. 2nd bending mode shape

Figure 11. 3rd bending mode shape

The third bending mode is not easily perceptible on either bearing due to the low modal displacement observed at both bearings, as discussed earlier and shown in Figure 11. For subcritical machines (operating speed is below the first bending

mode) on magnetic bearings with no perceived super-synchronous excitation source beyond the magnetic bearings, there is generally no detrimental effect to having a low modal displacement at the bearings. In the case of the PLD expander-generator, there is no expected excitation source for supersynchronous forces. The seals used for the PLD expander-generator will impart cross-coupled stiffnesses to the rotor, but these will generally manifest as a subsynchronous excitation to the rotor.

In addition to the 2 bending modes seen in the plant transfer function, there is a mode near 1513 Hz.

Figure 13 shows the corresponding sensitivity transfer function for both radial bearings at 0 rpm. The sensitivity gain on all modes is less than 10.5 dB, with peak sensitivities occurring in the 80-150 Hz range for the radial channels and the 55-85 Hz range for the axial channel. Although this exceeds the 9.5 dB Zone A requirement of ISO 14839-3 [9], the local maxima in the sensitivity transfer functions between 50 Hz and 300 Hz are associated with the relatively flexible factory test support and will not be present in the field installation. The compensation will be adjusted during field commissioning to meet the Zone A requirement if necessary.
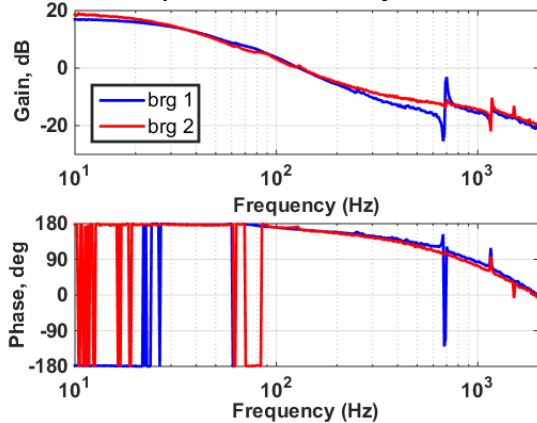

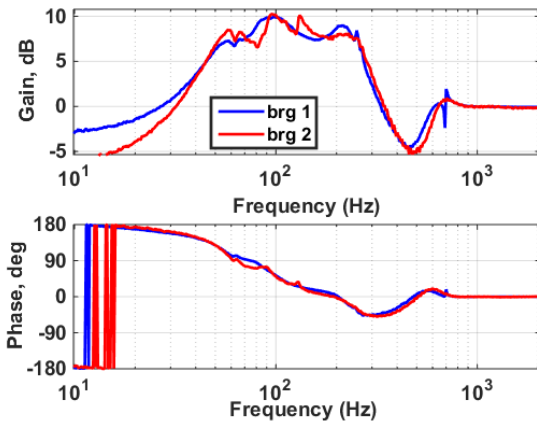Figure 12. Extended plant transfer function for radial bearings at 0 rpm

Figure 13. Sensitivity transfer function for radial bearings at 0 rpm

The magnetic bearing compensator was designed to either damp out the bending mode frequencies or to not respond (low stiffness) to excitations corresponding to the three bending mode frequencies seen in the plant transfer functions in Figure 12. As such, there is very little response seen at the bending modes in the sensitivity transfer functions.

Figure 14 shows the radial extended plant transfer function at 30,000 rpm. The three bending modes split into forward-whirl and backward-whirl bending modes, as seen in the Campbell diagram in Figure 7 earlier. Additionally, a large peak at 500 Hz is seen, corresponding to the speed of the rotor.

Figure 15 shows the corresponding radial sensitivity transfer functions at 30,000 rpm. The figure shows several local maxima between 50 Hz and 30 Hz, similar to those seen earlier in Figure 12. Again, these peaks can be attributed to modes associated with the test setup. As with the sensitivity transfer function at 0 rpm, the sensitivity transfer function at 30 krpm shows little response near the bending modes frequencies.
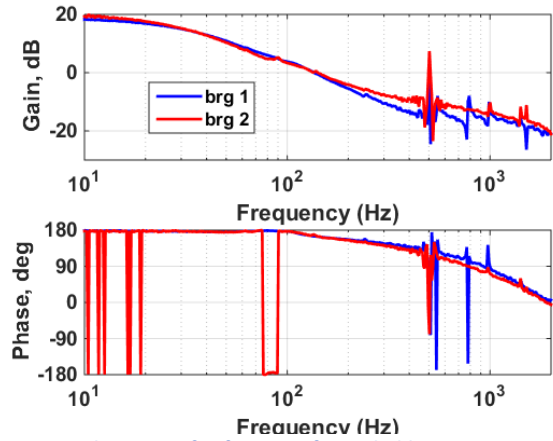

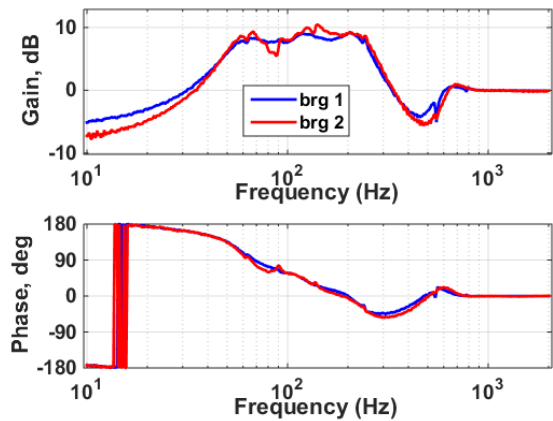Figure 14. Plant transfer function for radial bearings at 30,000 rpm

Figure 15. Sensitivity transfer function for radial bearings at 30,000 rpm

A Campbell diagram was constructed from the modes observed in measured plant transfer functions taken at various

6

speeds from 0-30,000 rpm. Figure 16 shows a comparison of the measured and predicted first two bending modes versus speed. The modes were generally well-predicted.
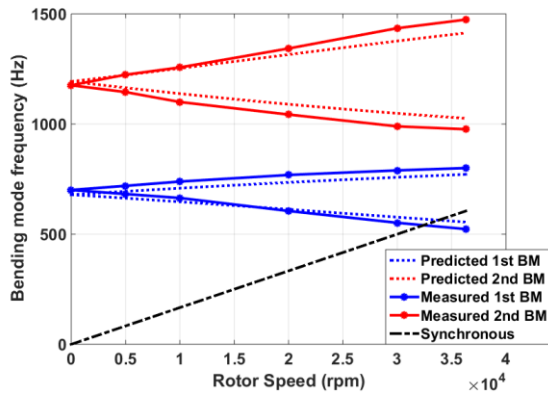

Figure 16. Measured and predicted free-free natural frequencies versus speed

BACKUP BEARING DESIGN AND DROP TEST RESULTS

The backup bearing selected for this application is a super-duplex, angular-contact hybrid rolling-element bearing. Figure 17 shows a partial cross-section of this bearing. The super-duplex ball bearing consists of two separate rows of balls, contained by two separate outer rings, and a single inner ring construction. The races are silver-plated and lubricated with a grease film.
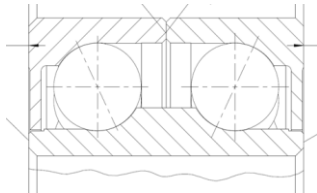

Figure 17. Typical "super-duplex" backup bearing

A series of drop tests was carried out to test the reliability of the backup bearings. All testing was done with a dummy impeller installed on the machine, such that significant thrust loads or torques will not be transmitted by the wheel. A brake resistor was used to decelerate the rotor during the drop tests. The rotor was decelerated while spinning on the backup bearings. The backup bearings were required to withstand five rotor drops at 31,500 RPM without spindown to 0 rpm without failing. Failure was defined as the inability to re-levitate the rotor following a test.

Prior to performing the drop tests, a series of progressive drops was carried out, wherein a rotor re-levitation was attempted after the rotor decelerated by 5,000 rpm. Table 5 summarizes the list of drop tests performed on the PLD expander. Due to the high deceleration rate, it was not possible to re-levitate the rotor at 5 krpm and 10 krpm. During drops 6-10, re-levitation was not attempted. During drop 5, re-levitation

was attempted at 20 krpm, but was not successful. A second re-levitation at 10 krpm was attempted and was successful. It is not always possible to re-levitate the rotor at all speeds, as the compensator is not tuned with consideration of the dynamics of the rotor supported by the backup bearings. If re-levitation at specific speeds is deemed to be a requirement, an "intermittent recovery compensator (IRC)" may be designed; this can be specifically tuned to recover the rotor, as described in Khatri et al. [10]. For this project, re-levitation at high speed is not considered a direct requirement.

Figure 18 shows an example of the y1 position during drop test #3 (15 krpm drop). As can be seen, the rotor experiences a transient motion for ~0.5 seconds while the inner ring accelerates to a steady-state speed. During this time period, the rotor motion can be characterized as "bouncing" around the bearing clearance space. The rotor then goes into full forward whirl for ~0.7 seconds before settling into a pendulum/rocking motion along one quadrant of the bearing. Finally, the rotor speed reaches 10 krpm, the rotor is re-levitated.

TABLE 5. LIST OF DROP TESTS PERFORMED

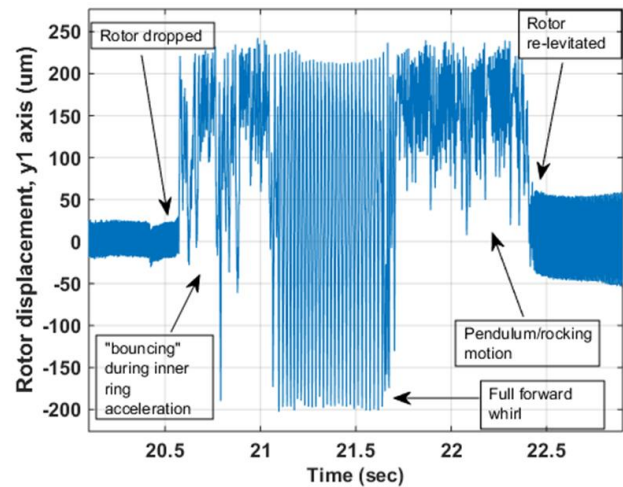| Drop #	Drop Speed (krpm)	Actual Pickup Speed (krpm)
1	5	No pickup
2	10	No pickup
3	15	10
4	20	15
5	25	10
6	31.5	No pickup
7	31.5	No pickup
8	31.5	No pickup
9	31.5	No pickup
10	31.5	No pickup

Figure 18. Y1 sensor position reading versus time during 15 krpm progressive drop

After each drop and spindown, the rotor-backup bearing clearance was checked to partially characterize the health of the bearing. The levitation currents were also checked to ensure the rotor-stator relative displacement had not changed. The backup bearings were deemed to have successfully survived all of the drops.

After the completion of the drop testing, the backup bearings were removed from the machine and inspected. The individual components of the bearing were disassembled and inspected under a microscope. Both bearings showed a mixture of clean grease and dark particles on the outer and inner races; the dark particles may be attributed to an outside contaminant or from worn silver. Figure 19 shows this mixture on the TE bearing outer race. After cleaning, both bearings showed minimal wear in the center of the ball path on the outer race but were otherwise free of wear caused by radial loading. Figure 20 shows the TE bearing outer race after cleaning. Most of the silver plating in both bearings was still intact. The TE bearing showed wear on the axial contact face of the inner ring, including a significant depletion of the silver coating, which was deemed normal given the number of drops. The bores of both bearing inner rings showed one fine circumferential line caused by contact between the inner ring bore and rotor.

The balls in both bearings showed a minor *wool-ball* effect, characterized by great circles caused by ball-to-ball contact at high speed. While this effect is typical for full-complement bearings, the amount of wear is small compared to other auxiliary bearing applications. Figure 21 shows a ball from the TE bearing showing this effect.

Figure 19. TE bearing outer race (post-drop test), with a mixture of fresh grease and dark particles

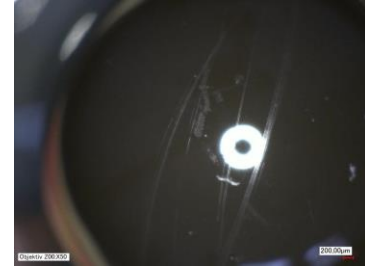Figure 20. TE bearing outer race after cleaning shows minimal wear

Figure 21. Ball from TE bearing, showing the "wool-ball" effect on the surface

Overall, both bearings were deemed to be in good condition, with the ability to sustain more drops.

AERODYNAMIC LOADING EFFECTS ON BEARING

Thrust loading in integrated machines is a primary topic of interest in industrial expanders, especially those supported by AMBs. To compensate the impeller thrust due to process load, a dedicated thrust balance system has been designed on the NDE side of the machine, using a single-effect piston. While a double-effect piston has a higher flexibility in terms of balancing capabilities, its geometry is generally more complex, increasing the overhung mass of the system and reducing the rotordynamic separation margin. This balancing feature is commonly used on expander compressor applications to limit static axial load on the thrust bearing [11].

The piston injects an external pressurized gas on the balance piston surface, causing an axial force towards the TE of the rotor. The pressure of the process gas is regulated by an active thrust balance system consisting of a control valve modulated through a feedback control algorithm implemented in the unit control system aimed at minimizing the current flowing through the AMB thrust coil. A diagram of the active thrust balance system is shown in Figure 22.
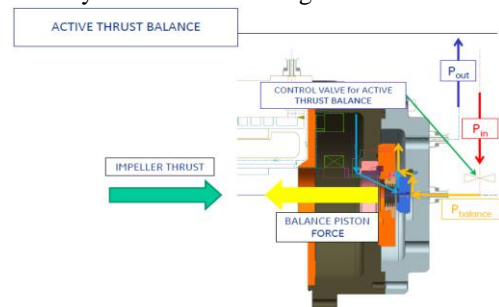

Figure 22. Active thrust balance system for PLD expander generator

An analysis was run to understand the effect of the expander aerodynamic loading on the thrust bearing:

1.) The first part of the analysis focuses on determining the maximum and minimum aerodynamic loads due to impeller unbalanced flow conditions.
2.) The second part of the analysis uses the calculated maximum/minimum thrust loads as inputs to a system thrust dynamics model, which includes the thrust

bearing dynamics and a transient thrust load profile. The system model is then used to analyze bearing loading/displacement during various shutdown conditions.

For the first analysis, individual contributions to the total thrust load were calculated through computational fluid dynamics (CFD) of the flow channel and an internal fluid network of cavities. A sensitivity analysis was performed to assess the effect of various wheel geometrical parameters on the total thrust load. The CFD analyses were performed using varied inlet mass flows and rotating speeds, such that a full flow path thrust map could be developed.

A similar analysis was carried out for the internal cavities and the back-wheel section to determine their contribution to the front-wheel thrust balance. There is a minor contribution from the flow momentum on the impeller hub which is included in the calculation.

The net load due to the internal flow is calculated by adding the individual contributions from the rotating cavities, gaps, labyrinth seal pockets, and bearing clearances, resolving the mass flow, pressure, and temperature for each branch of the system. All the calculated pressures from the individual rotor sections are multiplied by the corresponding rotating surface areas defining the related thrust force.

The individual rotor sections/components, which were analyzed for their contribution to the total thrust load are shown in Figure 23. The value of individual thrust load contributions for a single example configuration is shown in Figure 24. Figure 24 can be used to understand what components contribute more to the total thrust load. The position of the back-wheel seal and the cavity pressure defines most of the balancing force, and the remaining balancing force is delivered by the piston. This keeps the piston small, allowing for better rotordynamic separation margin.
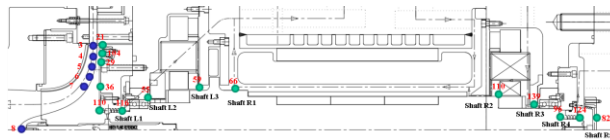
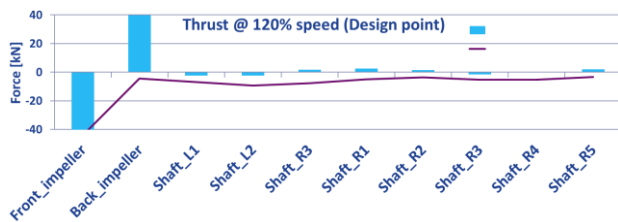

Figure 23: Pressure sensors

Figure 24: Individual thrust load contributions from various shaft sections for one example case

Another important aspect is the sensitivity of the cavity pressures and hence cavity thrust load contributions to: 1) variations in the individual seal clearances, 2) variation of the impeller inlet pressure, and 3) variation of the balance piston

inlet pressure. A sensitivity study, summarized in Table 6, showed that the most influential parameters on thrust load were the clearances of the seals behind the impeller. The impeller inlet pressure, balance piston hole pressure.

There are three results that are evaluated for the proper design of the thrust balancing system so that the thrust bearing load capacity is not exceeded:

1.) P_{cv} (**pressure @ balancing valve close**): minimum balancing force

2.) P_d (**pressure @ design**): nominal (zero) balancing force

3.) P_o (**pressure @ balancing valve opened**): maximum balancing force

The uncertainty range derived from the variability of the geometrical parameters mentioned earlier and shown in Figure 25 is included in the final (steady state) thrust calculation.

TABLE 6. EFFECT OF MECHANICAL TOLERANCES ON THRUST LOAD

	Dimension Value			Thrust Load (kN)			
	Min Dim	Nom Dim	Max Dim	At Min Dim	At Nom Dim	At Max Dim	|Max-Min|/ Nom
Impeller inlet pressure (MPa)	1.14	1.17	1.20	-1.75	-1.80	-1.87	6.7%
Pressure in Balance holes (MPa)	0.72	0.73	0.74	-1.75	-1.80	-1.87	6.7%
Clearance Laby High R (mm)	0.22	0.28	0.32	-1.92	-1.88	-1.65	14.4%
Clearance Laby Low R (mm)	0.22	0.29	0.40	-1.59	-1.80	-2.50	50.6%
Clearance Wheel Seal (mm)	0.20	0.26	0.32	-1.80	-1.80	-1.81	0.6%
Clearance Bearing Seal (mm)	.214	.332	.430	-1.87	-1.79	-1.77	5.6%
Clearance Thrust Seal (mm)	.231	.26	.290	-1.85	-1.82	-1.75	5.5%

The second part of this analysis evaluates the effects of the thrust load during various Emergency Shut Down (ESD) and trip scenarios. A dynamic model was developed using Matlab/Simulink®, as shown in Figure 26. The block *H(s)* is a closed loop LTI model with axial rotor force as the input and axial rotor displacement as the output. The axial magnetic bearing sensor, compensator, amplifier and actuator gain are in the feedback path of the LTI model.

The maximum and minimum absolute thrust loads from the sensitivity study were used as the initial thrust loads. Three different transient load conditions have been simulated:

1.) ESD with fast deceleration:
In the ESD scenario, the machine is stopped, while the rotor is spinning at full speed. This would be the typical scenario during a system failure. A resistor load bank (brake resistor, BR) is used to brake the rotor quickly.

2.) Trip with fast deceleration:
In this overspeed trip scenario, the machine is stopped, while the rotor is spinning at 103% of full speed. A resistor load bank is used to brake the rotor quickly.

3.) Trip without fast deceleration:
In this overspeed trip scenario, the machine is stopped, while the rotor is spinning at 103% of full speed. The rotor coasts down to 0 rpm due to windage and other losses in the system.
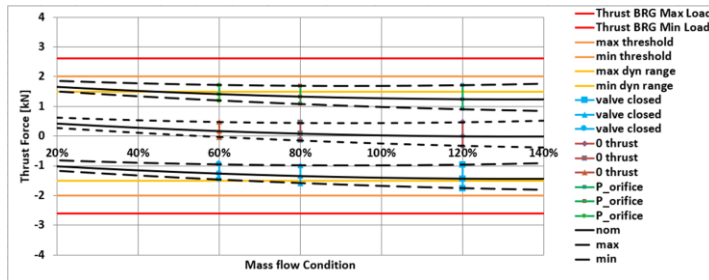

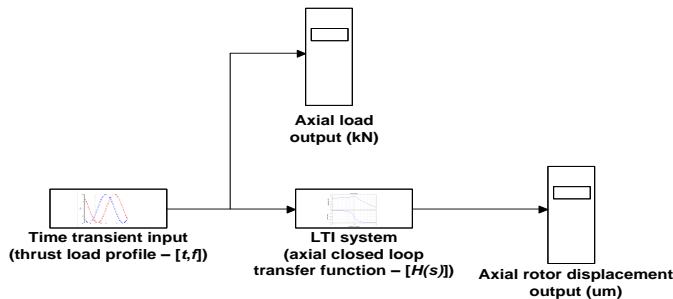**Figure 25. Thrust Force range with uncertainties**

Figure 26. Matlab/Simulink® model for axial transient dynamic simulation

An estimation of the thrust load profile (force vs. time) was calculated based on the speed profile (speed vs. time) for each scenario. The thrust load profile was used as an input to the thrust bearing closed-loop transfer function to obtain the axial displacement. The simulation results confirm the capability of the system to withstand the load during these transient scenarios, which represent the peak axial displacements due to aerodynamic loading.

The thrust load versus time curves for all scenarios are shown in Figure 27. The axial displacement versus time curves for all scenarios are shown in Figure 28.

The worst-case scenario is the trip-without-braking-resistor scenario, where the initial axial load is approximately -1.8 kN. In this scenario, the thrust bearing would be overloading, likely resulting in a hard landing on the backup bearings. The use of a braking resistor slightly reduces the amplitude of the thrust load, hence it is recommended to use this during a trip event if no other drawbacks are present. The simulation does not include the effect of the thrust balancing system dynamics. To avoid risk of a hard landing, it is recommended to operate the machine with a 0.3kN initial thrust load (axial unbalance), in order to initiate the trip with a lower thrust load. By using a thrust balance system, the bearing will not be overloaded under the worst-case aerodynamic loading conditions.
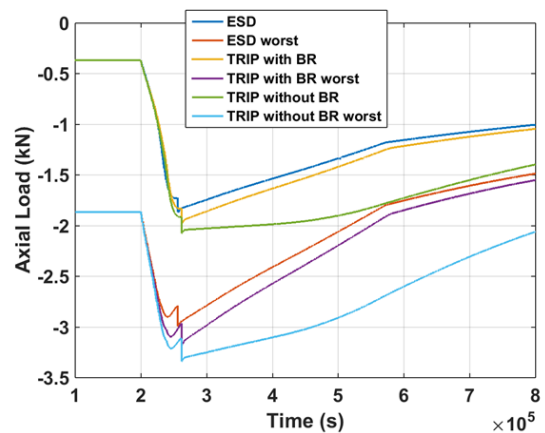

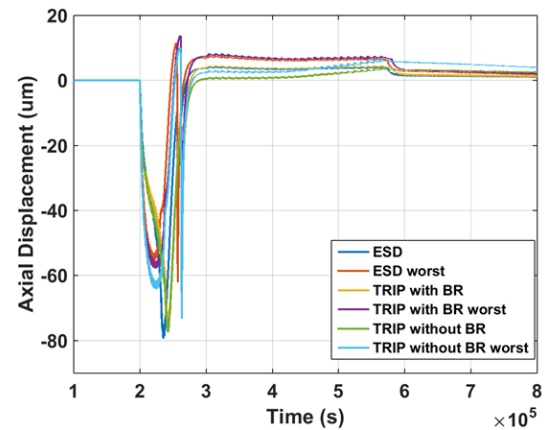**Figure 27. Axial transient simulation result (load)**

Figure 28. Axial transient simulation result (displacement)

CONCLUSIONS AND FUTURE WORK

A 300 kW integrated and fully sealed turboexpander-generator for natural gas pressure letdown (PLD) was developed by Baker Hughes, General Electric (BHGE), in conjunction with Calnetix Technologies. This paper described

the design and analysis of the generator, magnetic bearings, and touchdown bearings, as well as a review of some test results from the prototype mechanical run tests, load tests, and backup bearing drop tests.

The prototype machine will be moved to a PLD station in Bologna, Italy, where it will be commissioned in 2019. A future technical paper may include field test results from the site commissioning and first several months of field operation.

REFERENCES

[1] Howard, C., Oosthuizen, P., Peppley B., **An Investigation of the Performance of a Hybrid Turboexpander-fuel Cell System for Power Recovery at Natural Gas Pressure Reduction Stations**, Applied Thermal Engineering, vol. 31, no. 13, pp. 2165-70, 2011.

[2] Swanson, E., Hawkins, L., Masala A. **New Active Magnetic Bearing Requirements for Compressors in API 617 Eighth Edition**, Proceedings of the 43rd Turbomachinery Symposium, Houston, Texas, September 2014.

[3] Filatov A., Hawkins L., **An Axial Position Sensor for Active Magnetic Bearings**, Proceedings of ASME Turbo Expo: Power for Land, Sea and Air, Glasgow, UK, June 2010

[4] Filatov, A., Hawkins, L., **Constant-Flux Edge Sensor,** Proceedings of the 13th International Symposium on Magnetic Bearings, Arlington, Virginia, USA, August 6-9, 2012.

[5] Filatov A. et al., **Magnetic Bearing Actuator Design for a Gas Expander Generator,** Proceedings of 9th International Symp. on Magnetic Bearings, Kentucky, USA, August 2004.

[6] Filatov, A., Hawkins, L., **Novel Combination Radial/Axial Homopolar Active Magnetic Bearing,** 1st Brazilian Workshop on Magnetic Bearings, Rio de Janeiro, Brazil, October 25-26, 2013.

[7] Hijikata, K., Takemoto, M., Ogasawara, S., Chiba, A., Fukao, T., **Behavior of a novel thrust magnetic bearing with a cylindrical rotor on high speed rotation,** IEEE Transactions on Magnetics, vol. 45, issue 10, pp. 4617-4620, 10/2009

[8] Bleuler, H., Cole, M., Keogh,P., Larsonneur, R., Maslen, E., Okada,Y., Schweitzer, G., Traxler, A. **Magnetic bearings: theory, design, and application to rotating machinery**, pp. 59-67 Springer: Berlin/Heidelberg, Germany, 2009.

[9] **ISO 14839-3:2006,** Mechanical vibration -- Vibration of rotating machinery equipped with active magnetic bearings -- Part 3: Evaluation of stability margin.

[10] Khatri R. et al., **Demonstrated Operability and Reliability Improvements for a Prototype High-Speed Rotary-Disc Atomizer Supported on Active Magnetic Bearings**, Proceedings of ASME Turbo Expo: Turbine Technical Conference and Exposition, Montreal, Canada, June 2015

[11] API 617 American Petroleum Institute, 2014, **API Standard 617, Eighth Edition, Axial and Centrifugal Compressors and Expander-Compressors**, Washington, D.C., USA, API Publishing Services